



Supporting Online Material for
**Geophysical Detection of Relict Metasomatism from an Archean
(~3.5 Ga) Subduction Zone**

Chin-Wu Chen,^{*} Stéphane Rondenay, Rob. L. Evans, David B. Snyder

^{*}To whom correspondence should be addressed. E-mail: cwchen@mit.edu

Published 20 November 2009, *Science* **326**, 1089 (2009)
DOI: 10.1126/science.1178477

This PDF file includes:

SOM Text
Figs. S1 to S4
Table S1
References

1 Observation and resolution of the central Slave seismic discontinuity

The seismic receiver function profile we present in Fig. 2 of the paper is constructed using *P*-to-*SV* (*Ps*) converted waves binned according to common conversion points at 100 km depth (*S1*) and source-normalized by simultaneous deconvolution (*S2*), thus providing a 2-D profile of seismic discontinuities relative to depth. The receiver function signals are caused by seismic impedance (product of density and seismic velocity) contrasts in Earth, but sensitivity tests show that in the context of lithospheric structure they are mostly sensitive to velocity variations (*S3*). Therefore, their amplitudes effectively represent seismic velocity contrasts. The velocity contrast of the Moho across the Slave craton is determined to be ~20% from a seismic refraction experiment (*S4*). The velocity contrast of the central Slave seismic discontinuity is thus estimated by comparing its amplitude with that of the Moho, and corresponds to 9-21%. These values corroborate the results from modeling of the converted *SV* signals, which imply a 6-23% velocity contrasts (*S5*).

To evaluate the nature and robustness of the central Slave seismic discontinuity, we construct *SV* and *SH* receiver function profiles using data from three different backazimuthal ranges (Fig. S1): 0-90° (NE), 90-180° (SE), and 270-360° (NW). The southwest quadrant (180-270°) contains only one event that does not yield a continuous and stable receiver function profile, thus it is excluded from the discussion. The *SV*-component profiles from all three quadrants indicate the presence of a low velocity discontinuity at ~100 km depth beneath the central Slave craton. The amplitude and lateral extent of the discontinuity varies from one quadrant to the other. This may reflect (i) variability in the number and quality of the events – the NW quadrant comprises 36 events, versus 18 and 4

for the SE and NE quadrants, respectively, (ii) rapid lateral variations in the properties of the discontinuity, or (iii) a combination of these two factors. To constrain the scale of possible lateral variations, we plot the conversion points of P_s waves converted at 100 km depth, with color coding corresponding to the different quadrants (Fig. S2). This exercise suggests that lateral variation must occur over scale-lengths of the order of ~ 20 km to account for discrepancies between quadrants. The discontinuity is clearest for the most populated (i.e., NW) quadrant and we therefore used the corresponding profile in Fig. 2. The SH -component profiles for the various quadrants (as well as for smaller backazimuthal bins – not shown) do not reveal any clear, coherent signals near 100 km depth beneath the central Slave. This suggests that the discontinuity observed in the SV profiles is not due to seismic anisotropy.

The uncertainty on the depth of the central Slave discontinuity is related mainly to the background velocity model and to the coherence between individual waveforms that are combined into stacks. To evaluate the depth uncertainty due to changes in the background velocity model, we generate depth-migrated receiver functions using models with different crustal and mantle V_P and V_P/V_S (Table S1), and determine the corresponding changes in depth of the 100 km discontinuity signal. A realistic range of V_P and V_P/V_S for the crust is determined on the basis of the aforementioned seismic refraction experiment (S4). Results from this experiment show that the crust comprises two layers: an upper layer (0-20 km depth) with V_P ranging between 6.35-6.55 km/s, and a lower layer (20-40 km depth) with V_P ranging between 6.7-6.9 km/s. The V_P values in the upper crustal layer correspond to a rock composition of metagabbro and greenschist with V_P/V_S of 1.78 (S6). For the lower

crust, the values of V_P correspond to felsic to mafic granulite with V_P/V_S of 1.78-1.9 (S6). For the upper mantle, the seismic velocities are estimated based on properties of lherzolitic and harzburgitic lithologies at pressure-temperature condition of the Slave lithosphere, giving a range in V_P of 7.7-8.3 km/s and a V_P/V_S ratio of 1.77-1.78 (S7). We derive four end-member models based on the estimated values of V_P and V_P/V_S (Table S1), and use these models to re-compute the receiver functions for the 8 bins in which the central Slave discontinuity is most clearly detected. The corresponding depth range of the discontinuity (i.e., the minimum of the negative impulse) is shown by a green line in Fig. S3, and implies an uncertainty of <10 km on the depth of the discontinuity.

To evaluate the depth uncertainty related to waveform coherence, we use the bootstrapping technique and estimate the 95% confidence interval on the depth of the discontinuity (Fig. S3). The bootstrap test is conducted on the bins that contain at least 10 converted waves. A population of receiver function waveforms is generated by simultaneously deconvolving groups of traces randomly selected from the original dataset (with replacement, up to the size of the original samples) and repeating the operation 100 times. For those bins that sample fewer than 10 waves, we simply display the individual receiver functions in conjunction with the simultaneously deconvolved waveform. This analysis indicates that variability between waveforms causes uncertainties of 2-10 km on the depth of the discontinuity. This test also yields an estimate of uncertainty on the amplitude of converted signal. From the bins that are amenable to bootstrapping, we find that the amplitude of the signal exhibits an error bar of ± 0.017 (normalized units) based on the 95% confidence interval, which translates into an uncertainty of 2.5-6% on the

magnitude of the S velocity anomaly.

2 Causes of the seismic and electrical discontinuities in the central Slave

Possible causes for both discontinuities include the existence of local gradients in temperature, composition or water content, and the presence of partial melt. In this section we investigate the effect of each of these factors on the seismic and electrical properties of the upper mantle.

2.1 Thermal anomaly

Experimental studies (S8) have shown that the thermal dependence of velocity can be described by the following expression:

$$\partial \ln V_S / \partial T = \partial \ln V_{SU} / \partial T - F(\alpha) [Q^{-1}(\omega, T) / \pi] (E + PV) / RT^2$$

where

$$Q^{-1} = A d^{-m} T_0^{\alpha} \exp(-\alpha(E + PV) / RT)$$

$$F(\alpha) = (\pi\alpha/2) \cot(\pi\alpha/2)$$

where V_S is the shear-wave velocity, T is the temperature, Q is the seismic quality factor, and $F(\alpha)$ is attenuation-dependent coefficient in which $F(\alpha) \rightarrow 1$ as $\alpha \rightarrow 0$. The parameter values are chosen from previous studies (S8-S10) and are conservative so as to yield the minimum possible temperature change: change in the unrelaxed shear-wavespeed with respect to temperature, $\partial \ln V_{SU} / \partial T = -8.6 \times 10^{-5} \text{ K}^{-1}$; activation energy, $E = 424,000 \text{ J/mol}$;

$A=730 \text{ s}^{-\alpha} \mu\text{m}^m$; grain size, $d=1\text{mm}$; frequency (ω) dependence of attenuation, $\alpha=0.26$; grain size sensitivity of attenuation, $m=0.26$; activation volume, $V=6 \times 10^{-6} \text{ m}^3/\text{mol}$; pressure, $P=3.16 \text{ GPa}$. The background temperature is set at $T=750^\circ\text{C}$ (*S11*) and the central period is $T_0=2 \text{ s}$.

If the observed seismic anomaly of 9-21% V_s reduction is to be explained solely by thermal effect, the required temperature increases are therefore calculated to be 1000-2200°C. Lab measurements (*S12*) on the Slave peridotite xenoliths also indicate that a temperature increase of $\sim 400^\circ\text{C}$ (assuming the background temperature to be $\sim 750^\circ\text{C}$) would be needed to explain the electrical anomaly. Such gradients are implausible in the context of a cold, depleted mantle root with a petrologically-inferred thermal gradient of $< 6^\circ\text{C}/\text{km}$ (*S11*), unless they were caused by a transient heating event such as a sudden injection of kimberlitic magma. However, the last kimberlite eruption occurred ~ 50 million years ago (*S13*, *S14*), much too long ago to explain the required, current day thermal anomalies.

2.2 Compositional anomaly

The main causes of compositional anomalies in cratonic environments are melt depletion, juxtaposition of different mantle terranes, and mineral alteration/deposition. Xenolith studies suggest that the lithosphere of the Slave craton exhibits varying degrees of depletion in iron and other magmaphile elements (*S13*). However, the largest depletion interface inside the lithosphere, which occurs at $\sim 150 \text{ km}$ in the central Slave, could account for at most $\sim 1\%$ shear-wavespeed anomaly (*S15*). Moreover, the effects of iron depletion on

electrical conductivity are negligible (only about one third of an order of magnitude) (*S16*). Therefore, melt depletion alone is not a viable candidate to explain the anomalies.

Juxtaposition of different mantle terranes is associated with possible mechanism of cratonic assembly and modification, such as underplating by flat subduction, plume head subcretion, and foundering of the lithospheric root. However, interfaces between such adjacent terranes (if one omits the effects of metasomatic alteration for the time being) result either in varying degrees of melt depletion, which as seen above is not a viable explanation, or in transitions between mantle peridotites and eclogitized oceanic crust, which are quasi-indistinguishable seismically (*S17, S18*) and electrically (*S19*). Interfaces between underplated terranes have been invoked to explain anisotropic discontinuities observed in the SW Slave craton (*S2*). However, the central Slave discontinuity does not require seismic anisotropy (Fig. S1), therefore an alternative mechanism may be required.

There is probably no single type of mineral deposit or alteration that can simultaneously explain both anomalies. However, the anomalies can be due to different minerals that stem from a unique process of metasomatic alteration. For the seismic anomaly, hydrated minerals such as phlogopite, chlorite and talc are the most likely candidates, because they are stable at P-T conditions corresponding to the location of the anomaly (*S20, S21, S22*), and are known to reduce seismic velocity (*S23, S24*). Strong supporting evidence for this hypothesis comes from analyses of xenoliths from the central Slave that identify a horizon of phlogopite bearing eclogites (~50 vol% phlogopite) at ~100 km depth (*S25*). Although phlogopite has been invoked to explain conductive anomalies in

the mantle (*S26*), these anomalies have much smaller magnitude than that observed here and there is no experimental data that shows that phlogopite may generate the 0.01-0.03 S/m anomaly observed in the central Slave (*S27*). Alternatively, a more favored mineral to explain conductive anomalies in the mantle is graphite (*S27, S28*). Very small quantities of graphite deposited as interconnected films along grain boundaries can increase the electrical conductivity by several orders of magnitude (*S28*). There are a few mantle xenoliths from the central Slave that contain small concentrations of graphite, although they are not the phlogopite-rich xenoliths (*S25*). However, it is possible that a thin lithospheric layer exhibiting high concentration of graphite may not be well-represented in the population of xenoliths entrained to the surface due to its high level of alteration and resulting friability (*S25*). Therefore graphite films can be retained as a possible candidate for the electrical anomaly. Mineral deposits can therefore explain the seismic and electrical anomalies, whereby the two types of minerals invoked could be related to a same process of metasomatic alteration by a fluid rich in carbon. This would be consistent with fluid cycle within a subduction zone complex where large quantities of sediments (source of C) are being subducted (*S29*).

2.3 Water

Water can lower both seismic velocities and electrical resistivity (*S30, S31*). Liquid water is unlikely to remain stable over periods of millions of years in a cold, stable cratonic lithosphere, as it would eventually react with surrounding rocks to form alteration minerals. Therefore its effects are not considered further. Alternatively, water present as hydrogen in

the structure of nominally anhydrous minerals is a factor that must be considered. In terms of seismic observations, water primarily reduces seismic velocities through anelastic effects (*S30*) – theoretical calculations suggest that increasing water content by an order of magnitude results in an increase in seismic attenuation by a factor of two. Based on the observed range in values that attenuation can take in the continental lithosphere (*S32*) and the relationship between attenuation and seismic velocities (considering water as the only cause of attenuation, i.e., omitting additional effects from temperature), it has been argued that water may cause at most 4.3% velocity reduction in the lithosphere (*S10*). This is not enough to explain the anomaly observed here, but it may very well contribute to it, especially in the framework of the hypothesis that the discontinuity is due to an alteration front caused by metasomatism. With regards to electrical conductivity, the Archean lithosphere is considered to be cold and dry (*S33*), and the Slave's upper mantle temperature is insufficient to provide high enough activation energy to induce hydrogen diffusion that would enhance electrical conductivity to the observed levels.

2.4 Partial melt

The last mechanism we investigate as a possible source for both anomalies is a layer of partial melt at 100 km depth in the lithosphere of the central Slave. Theoretical calculations show that a very small quantity of partial melt (<3%) is sufficient to explain both the observed seismic velocity drop (*S34*) and electrical conductivity increase (*S35*). However, the Slave mantle temperature inferred from steady-state geotherm (*S11*) is much below the minimum solidus temperature under water saturation conditions (*S21*). Moreover, as

observed in section 2.1, it appears unlikely to sustain a thermal perturbation required to induce partial melting at the depth of observed anomalies.

2.5 Summary

In summary, we find that the most probable mechanism that can explain the coincident seismic and electrical anomalies below the central Slave craton is a metasomatic alteration front. In this model, the addition of fluids rich in carbon has caused mineral alteration into phlogopite, which is responsible for the seismic discontinuity, and the deposits of graphite, which lower the electrical resistivity.

3 Subduction models for the assembly of the central Slave craton

We propose two possible subduction scenarios that can explain the observed geophysical and petrological features, and result in the assembly of the block forming the central Slave craton, as depicted in Fig. S4.

References

1. K. G. Dueker, A. F. Sheehan, *J. Geophys. Res.* **102**, 8313 (1997).
2. M. G. Bostock, *J. Geophys. Res.* **103**, 21183 (1998).
3. C. A. Rychert, S. Rondenay, K. M. Fischer, *J. Geophys. Res.* **112**, 10.1029/2006JB004619 (2007).
4. G. Fernandez Viejo, R. M. Clowes, *Geophys. J. Int.* **153**, 1 (2003).

5. M. Moorkamp, A. G. Jones, D. W. Eaton, *Geophys. Res. Lett.* **34**,
10.1029/2007GL030519 (2007).
6. W. S. Holbrook, W. D. Mooney, N. I. Christensen, in *Continental Lower Crust*, D. M. Fountain, R. Arculus, R. W. Kay, Eds. (Elsevier, Amsterdam, 1992) vol. **43**, 1-43.
7. B. R. Hacker, G. A. Abers, S. M. Peacock, *J. Geophys. Res.* **108**, 2029,
10.1029/2001JB001127 (2003).
8. I. Jackson, J. D. Fitz Gerald, U. H. Faul, B. H Tan, *J. Geophys. Res.* **107**,
10.1029/2001JB001225 (2002).
9. D. G. Isaak, *J. Geophys. Res.* **97**, 1871 (1992).
10. C. A. Rychert, K. M. Fischer, S. Rondenay, *Nature* **436**, 542 (2005).
11. M. G. Kopylova, G. Caro, *J. Petrol.* **45**, 1045 (2004).
12. N. S. Bagdassarov, M. G. Kopylova, S. Eichert, *Phys. Earth Planet. Inter.* **161**, 126
(2007).
13. W. L. Griffin *et al.*, *J. Petrol.* **40**, 705 (1999).
14. D. B. Snyder, G. D. Lockhart, *J. Geol. Soc.* **162**, 737 (2005).
15. M. G. Kopylova, J. Lo, N. I. Christensen, *Lithos* **77**, 493 (2004).
16. A. G. Jones, R. L. Evans, D. E. Eaton, *Lithos* **109**, 131 (2009).
17. S. Rondenay, M. G. Bostock, J. Shragge, *J. Geophys. Res.* **106**, 30795 (2001).
18. S. Rondenay, G. A. Abers, P. E. van Keken, *Geology*, **36**, 275 (2008).
19. G. Heinson, S. Constable, *Geophys. J. Int.* **110**, 159 (1992).
20. D. J. Frost, *Rev. Mineral. Geochem.* **62**, 243 (2006).
21. T. L. Grove, N. Chatterjee, S. W. Parman, E. Medard, *Earth Planet. Sci. Lett.* **249**, 74
(2006).
22. A. R. Pawley, B. J. Wood, *Am. Mineral.* **80**, 998 (1995).
23. B. R. Hacker *et al.*, *J. Petrol.* **46**, 1661 (2005).

24. D. Mainprice, Y. Le Page, J. Rodgers, P. Jouanna, *Earth Planet. Sci. Lett.* **274**, 327 (2008).
25. S. Aulbach, N. J. Pearson, S. Y. O'Reilly, B. J. Doyle, *J. Petrol.* **48**, 1843 (2007).
26. D. E. Boerner *et al.*, *Science* **283**, 668 (1999).
27. A. G. Jones *et al.*, *Geology* **29**, 423 (2001).
28. M. Mareschal, W. S. Fyfe, J. Percival, T. Chan, *Nature* **357**, 674 (1992).
29. D. M. Kerrick, J. A. D. Connolly, *Nature* **411**, 293 (2001).
30. S. Karato, *Proc. Japan Academy* **71**, 61 (1995).
31. S. Karato, *Nature* **347**, 272 (1990).
32. Y. Gung, B. Romanowicz, *Geophys. J. Int.* **157**, 813 (2004).
33. G. Hirth, R. L. Evans, A. D. Chave, *Geochem. Geophys. Geosys.* **1**, 10.1029/2000G000048 (2000).
34. W. C. Hammond, E. D. Humphreys, *J. Geophys. Res.* **105**, 10975 (2000).
35. J. J. Roberts, J. A. Tyburczy, *J. Geophys. Res.* **104**, 7055 (1999).
36. W. J. Davis, A. G. Jones, W. Bleeker, H. Grütter, *Lithos* **71**, 575 (2003).
37. K. J. Westerlund *et al.*, *Cont. Mineral. Petrol.* **152**, 275 (2006).
38. D. B. Snyder, *Tectonics* **27**, TC4006, 10.1029/2007TC002132 (2008)

Supporting figure captions

Fig. S1.

SV- and *SH*-component receiver function profiles constructed by simultaneous deconvolution of converted *P*-to-*S* (*Ps*) waves binned according to common conversion points along line A-A' (Fig. 1), using data from (A) NW; (B) NE; and (C) SE quadrants. Red and blue colors represent positive (downward slow-to-fast) and negative (downward

fast to slow) seismic velocity contrasts, respectively. In all three *SV* components, a coherent positive discontinuity corresponding to the Moho is observed across the entire array at ~40 km depth, and a negative discontinuity is observed at ~100 km depth below the central Slave (green arrows). No clear coherent signal is observed across the array in the *SH* profile.

Fig. S2.

P_s conversion points at 100 km depth for events from the NW (magenta), NE (blue), SW (yellow), and SE (green) quadrants. The red points denote the conversion points from NW events for which the low-velocity discontinuity is observed.

Fig. S3.

Depth and amplitude uncertainty of the central Slave seismic discontinuity. Each panel shows *SV* receiver functions (in blue), simultaneously deconvolved and stacked, for the 8 bins at 100 km depth in which the discontinuity is observed. The central latitude of the bins is indicated above each panel, along with the number of waves contributing to each bin (in parentheses). In bins containing more than 10 events, a 95% confidence interval for the resulting receiver functions was obtained by bootstrapping, and is indicated by grey lines. For those bins that sample fewer than 10 waves, we display the individual receiver functions (grey dashed lines) to provide a visual assessment of the inter-trace variability. Note that these receiver functions are individually normalized. The red triangles indicate the depth of the discontinuity estimated from the receiver functions. The green lines denote

the range of depths obtained by recalculating the receiver functions for a range of possible background velocity models (Table S1). The magenta lines represent the 95% confidence interval on the depth estimate of the central Slave discontinuity based on bootstrapping.

Fig. S4.

Two models of cratonic assembly by subduction that explain the seismic-electrical discontinuity in the central Slave's lithosphere. The tectonic elements of each model are assigned to petrological horizons (labeled axis to the left of both panels) inferred from mantle xenoliths (13, 25). LAB: Lithosphere-asthenosphere boundary. **(A)** Accretion of a subducted slab at the base of a pre-cratonic lithosphere. The seismic-electrical discontinuity is associated with the interface between the proto-lithosphere and the altered crust of the subducted slab, while the ultra-depleted layer (UDL) represents the subcrustal lithospheric portion of this slab (13). An additional subcretion event involving subduction (2) and/or a mantle plume (13) is required in this model to account for the lower layers of the cratonic lithosphere. **(B)** Low-angle subduction beneath the pre-cratonic lithosphere. The seismic-electrical discontinuity is associated with the interface between the base of the proto-lithosphere and a layer of crystallized and metasomatized partial melt. The UDL is due to extensive melting in the mantle wedge (36). The lower eclogitic and lherzolitic layers represent the crust and mantle of the subducted slab. The inferred subduction event (either **A** or **B**) led to the assembly of a proto-cratonic lithosphere that was at least 150 km thick by 3.5 Ga, based on peridotitic diamonds found in the UDL (37). We propose that the central Slave comprises a broken fragment of this proto-craton (see vertical broken lines), which was aggregated to other continental fragments during the Neoproterozoic assembly of

the Slave craton (36, 38).

Table S1. End-member models used to estimate the uncertainty on the discontinuity depth due to the background velocity model. Last column shows values for the bin centered at 64.97°N.

Model	Upper crust		Lower crust		Mantle		Discontinuity depth (km)
	V_P (km/s)	V_P/V_S	V_P (km/s)	V_P/V_S	V_P (km/s)	V_P/V_S	
1	6.35	1.78	6.7	1.9	7.7	1.77	100
2	6.35	1.78	6.7	1.9	7.7	1.78	98
3	6.55	1.78	6.9	1.78	8.3	1.77	108
4	6.55	1.78	6.9	1.78	8.3	1.78	106

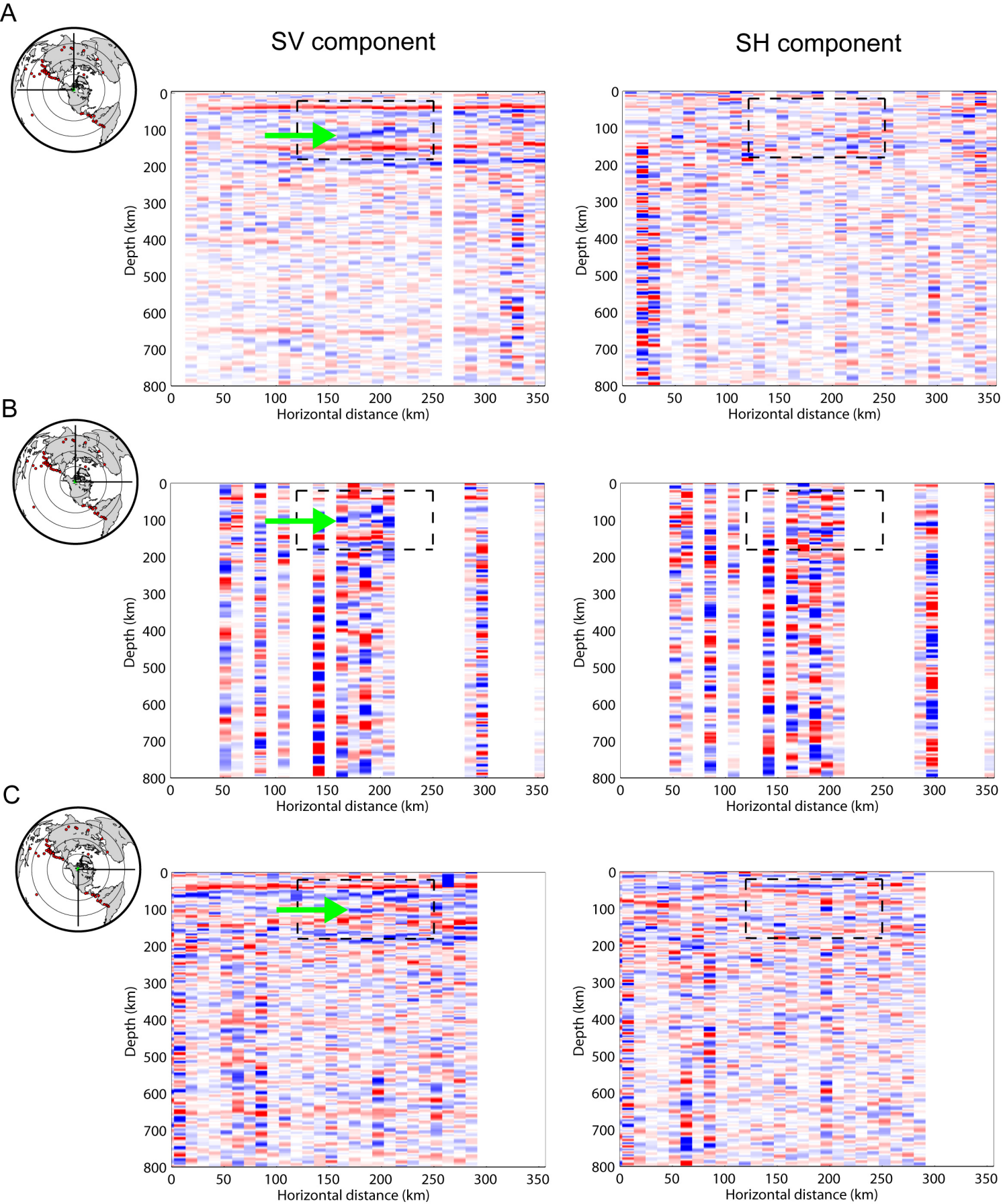


Fig. S1

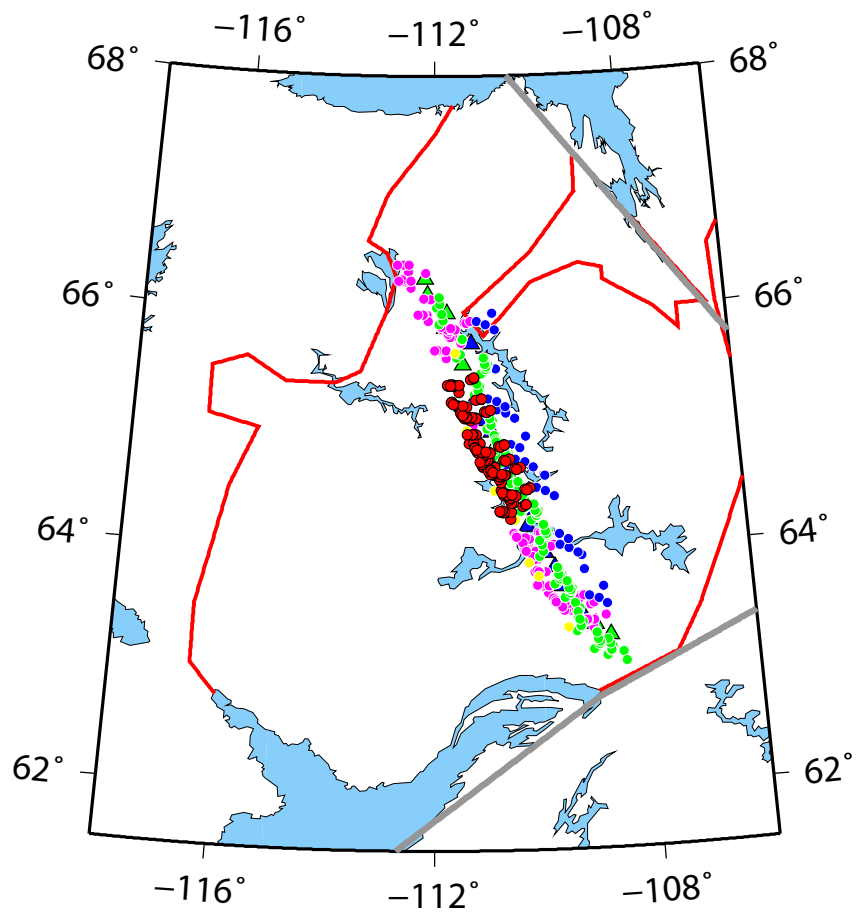


Fig. S2

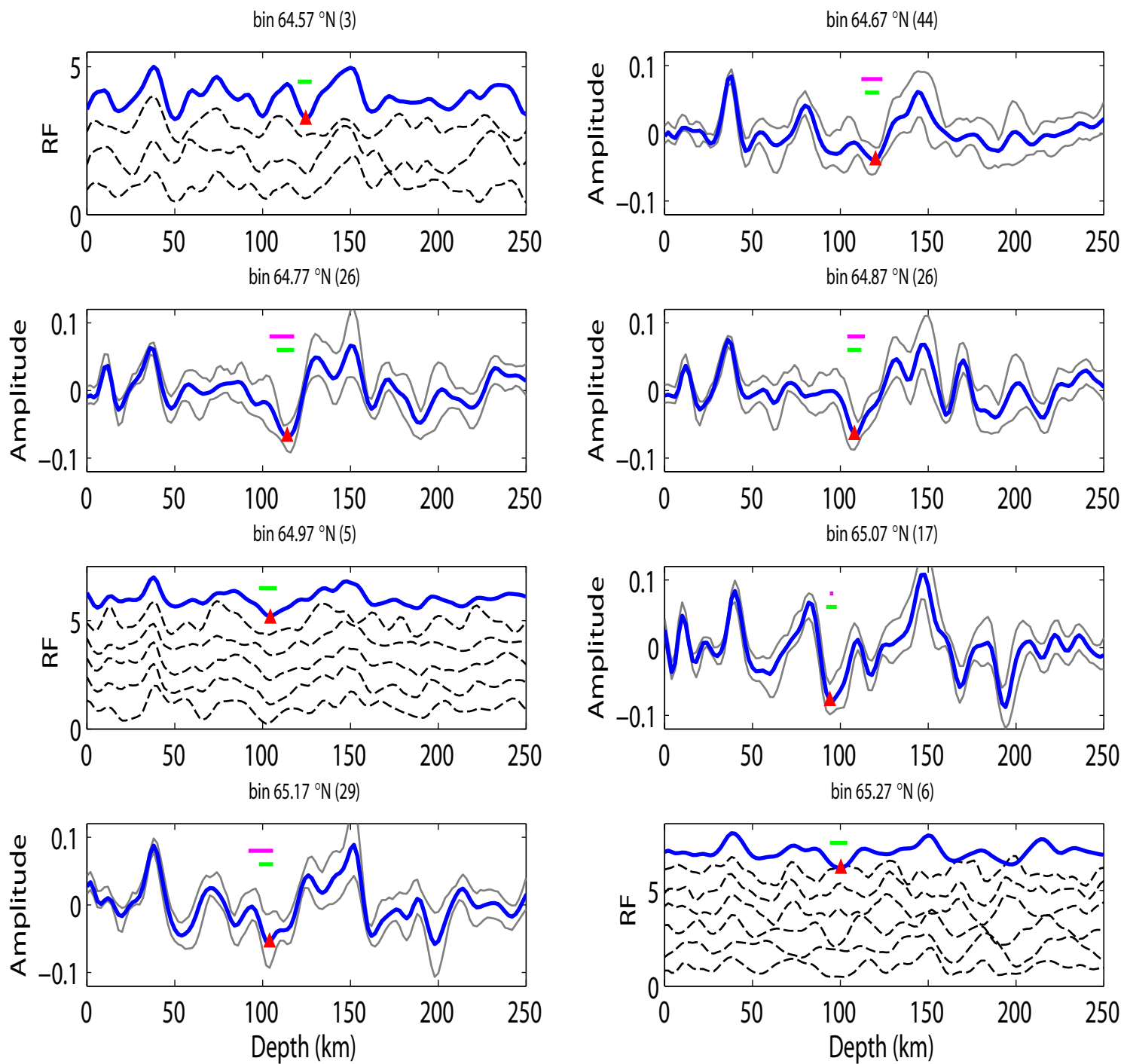


Fig. S3

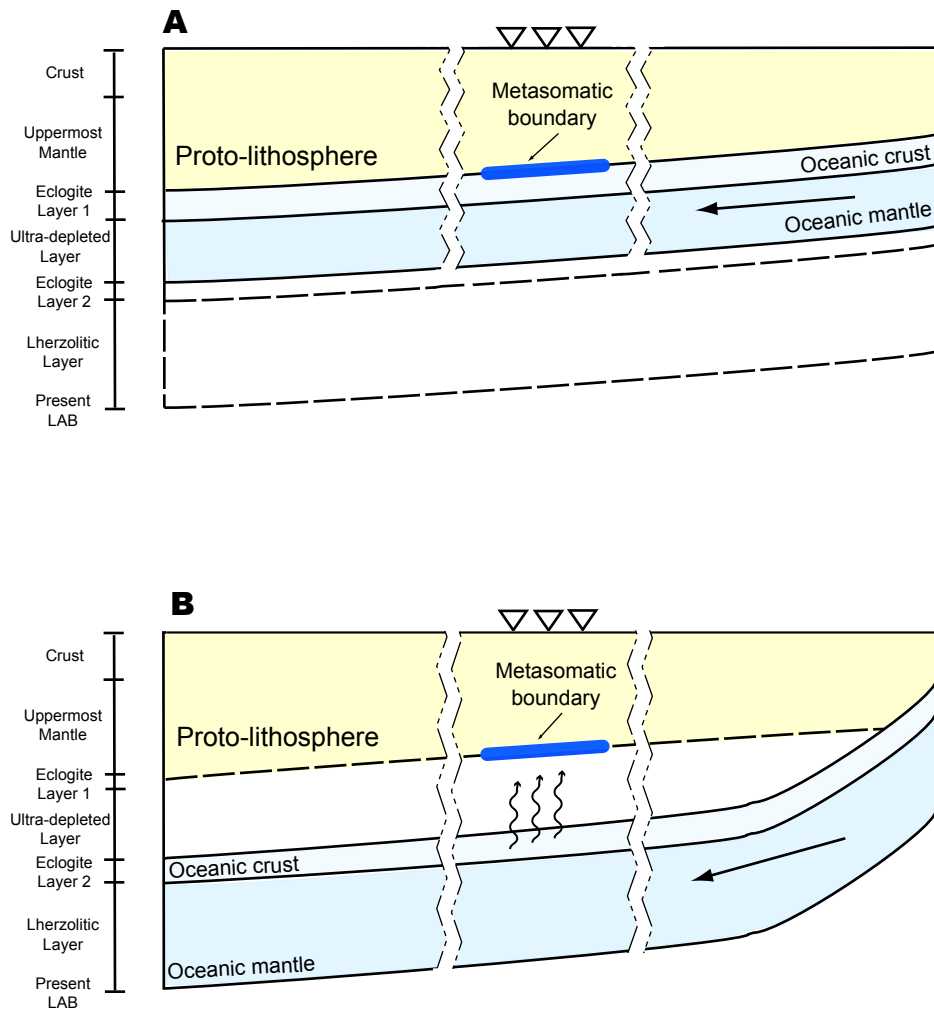


Fig. S4